



# Aerobic Alcohol Oxidation by a Zeolitic Octahedral Metal Oxide based on Iron Vanadomolybdates Under Mild Conditions

Qianqian Zhu,<sup>[a]</sup> Shanshan Yin,<sup>[a]</sup> Mengyuan Zhou,<sup>[a]</sup> Jie Wang,<sup>[a]</sup> Chaomin Chen,<sup>[a]</sup> Panpan Hu,<sup>[a]</sup> Xizhuo Jiang,<sup>[a]</sup> Zhenxin Zhang,<sup>\*,[a]</sup> Yanshuo Li,<sup>\*,[a]</sup> and Wataru Ueda<sup>[b]</sup>

Zeolitic octahedral metal oxides are fully-inorganic crystalline materials with the multi-component redox property and the intrinsic microporosity. The redox active zeolitic iron vanadomolybdate acts as a catalyst for aerobic oxidation of primary aromatic alcohols. Molecular oxygen is able to be activated in the material due to the confinement effect of the micropore

and the unique redox property of the framework. Different primary aromatic alcohols are oxidized by the material, and high alcohol conversion and aldehyde selectivity are achieved. The material is stable and able to be reused for 5 times without loss of activity.

## Introduction

Selective alcohol oxidation is important not only for green organic synthesis but also for industrial procedures, because the products such as esters, carboxylic acids, ketones, and aldehydes, are widely used in the fields of fine chemicals, commercial products, and polymer industries.<sup>[1]</sup> Molecular oxygen is one of the best oxidants for alcohol oxidation, because molecular oxygen is an inexpensive, abundant, and easily available oxidant. Although molecular oxygen is an ideal oxidant for oxidation, its activation is difficult due to the high stability. Therefore, to realize the activation of molecular oxygen is a key step for selective alcohol oxidation.

There are catalysts being used for heterogeneous aerobic oxidation of alcohol, such as supported noble metals,<sup>[2]</sup> Ru-based metal oxides,<sup>[3]</sup> inorganic-organic hybrids,<sup>[4]</sup> other metal oxides,<sup>[5]</sup> and Mo–V based oxides.<sup>[6]</sup> Among the reported

materials, Mo–V based metal oxides are interesting because the materials are noble metal free materials.

Zeolitic transition metal oxides are microporous crystalline metal oxides composed of metal-oxygen octahedra, which are also called zeolitic octahedral metal oxides (ZOMOs). ZOMOs are new fully-inorganic porous materials, and the construction of the framework is similar to that of metal organic framework (MOF), which is formed by assembly of metal-oxygen clusters as building blocks and inorganic ions as linkers (Figure 1a). The micropores are occupied by guest molecules and are able to be opened. ZOMOs have both advantages of transition metal oxides and microporous materials, showing not only the multi-electron redox property but also the intrinsic microporosity. Combined with the redox property and the confinement effect of the micropores, the materials show application potentials in many fields particularly in catalytic oxidations.

However, the examples of ZOMOs are not many, and the synthesis is difficult. The assembly of polyoxometalates (POMs) that act as ideal building blocks is a good methodology for obtaining ZOMOs.<sup>[7]</sup> There are different ZOMOs being synthesized by this approach for catalytic oxidation, such as pentagon unit based MoVO,<sup>[8]</sup> hexagon unit based WPO,<sup>[9]</sup> cubane unit based WVO,<sup>[10]</sup> and  $\epsilon$ -Keggin POM based material.<sup>[11]</sup>

Among these ZOMOs, the materials based on  $\epsilon$ -Keggin POMs are formed by assembly of  $\epsilon$ -Keggin POM with inorganic ions in a tetrahedral manner (Figure 1). The materials show high elemental diversity and is able to incorporate different elements such as Mo, V, Bi, Zn, Mn, Fe, and Co in the frameworks and to incorporate alkali metal ions and alkali earth metal ions as cation species,<sup>[12]</sup> forming various iso-structural compounds with different elemental compositions. Among these iso-structural materials,  $(\text{NH}_4)_2\text{Fe}^{\text{II}}_{0.6}\text{H}_{11.7}[\text{Fe}^{\text{II}}_{2.0}\text{Mo}^{\text{VI}}_{1.1}\text{Mo}^{\text{V}}_{10.9}\text{O}_{40}]$  and  $(\text{NH}_4)_2\text{Fe}^{\text{II}}_{0.6}\text{H}_{8.5}[\text{Fe}^{\text{II}}_{1.0}\text{Mo}^{\text{VI}}_{2.7}\text{Mo}^{\text{V}}_{8.9}\text{V}^{\text{IV}}_{1.4}\text{O}_{40}]$ , denoted as **NH<sub>4</sub>MoFeO** and **NH<sub>4</sub>MoFeVO**, are interesting. The Fe and Mo based ZOMOs can activate molecular oxygen at room temperature.<sup>[13]</sup> Therefore, we assume that the material based on the similar

[a] Prof. Q. Zhu, S. Yin, M. Zhou, J. Wang, C. Chen, P. Hu, X. Jiang, Prof. Z. Zhang, Prof. Y. Li  
School of Materials Science and Chemical Engineering,  
Ningbo University  
Fenghua road 818  
Ningbo  
Zhejiang, 315211 (P.R. China)  
E-mail: zhangzhenxin@nbu.edu.cn  
liyanshuo@nbu.edu.cn

[b] Prof. W. Ueda  
Faculty of Engineering  
Kanagawa University  
Rokkakubashi  
Kanagawa-ku  
Yokohama-shi  
Kanagawa, 221-8686 (Japan)

 Supporting information for this article is available on the WWW under <https://doi.org/10.1002/cctc.202001696>

 This publication is part of a Special Collection on "Supported Nanoparticles and Single-Atoms for Catalysis: Energy and Environmental Applications". Please check the ChemCatChem homepage for more articles in the collection.

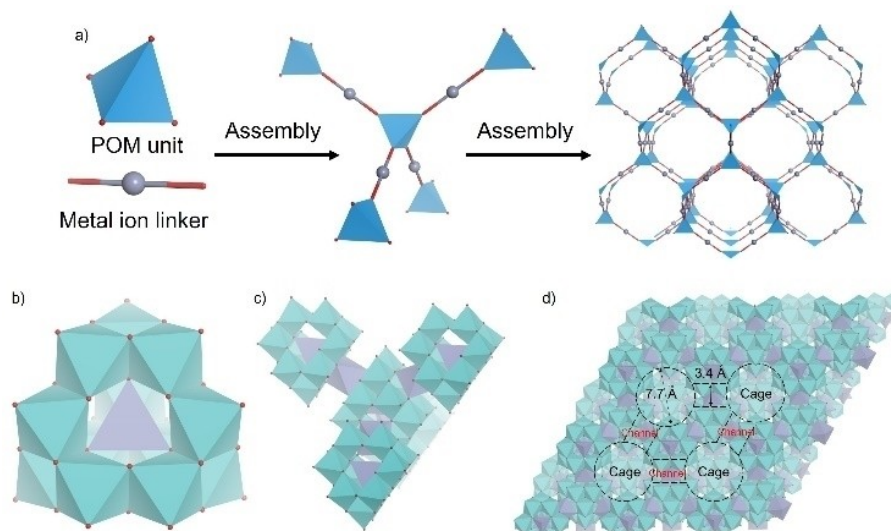


**Figure 1.** a) schematic representation of the assembly of ZOMOs by POM unit and linker. Structure modes of b)  $\epsilon$ -Keggin POM unit, c) connection of  $\epsilon$ -Keggin POM unit with metal ion linker, and d) the micropore system of the material, Mo or V (blue), Fe (purple), O (red).

compositions are active for the low temperature catalytic oxidation of organic compounds.

Herein, we reported the redox active zeolitic iron vanadomolybdate (**MoFeVO**) based on  $\epsilon$ -Keggin  $[\text{Fe}^{\text{III}}_{1.82}\text{Fe}^{\text{II}}_{0.18}\text{Mo}^{\text{V}}_{11.5}\text{V}^{\text{V}}_{0.3}\text{V}^{\text{IV}}_{0.7}\text{O}_{40}]^{12.38-}$  with Fe and V linkers and the unique redox property led to the catalytic performance for the aerobic oxidation of aromatic alcohols under mild conditions.  $\text{O}_2$  adsorbed in the micropores of the material at room temperature, which was confined and activated, causing oxidation of the material. V improved the redox activity of the material and increased the  $\text{O}_2$  adsorbed amount. The material catalyzed the oxidation of the aromatic alcohols to the aldehydes using air as an oxidant. The material was able to be recovered and reused for 5 times without loss of activity.

## Results and Discussion

### Material synthesis

**MoFeVO** and **MoFeO** were synthesized by the hydrothermal method, which was basically the same to the reported method with slight modification.<sup>[13]</sup> Herein,  $\text{Na}_2\text{MoO}_4 \cdot 2\text{H}_2\text{O}$  and  $\text{NaVO}_3$  were used as the Mo source and the V source, respectively, to produce the resulting materials with  $\text{Na}^+$  as the cation. The as-synthesized **MoFeVO** and **MoFeO** were characterized by powder X-ray diffraction (XRD) (Figure S1Aa,b), which demonstrated that the crystal structures of the materials were basically the same. They were typical iso-structural materials.

Elemental analysis showed that  $\text{Na}:\text{Mo}:\text{Fe}:\text{V}=1:11.5:2:1$  and  $1.5:12:2.5:0$  for **MoFeVO** and **MoFeO**, respectively, which indicated that V substituted both Mo and Fe in **MoFeVO**, because Mo and Fe ratios of **MoFeVO** decreased compared with those of **MoFeO**. Oxidation states of Mo from X-ray photoelectron spectroscopy (XPS) analysis were  $\text{Mo}^{\text{V}}$  for both

**MoFeVO** and **MoFeO**, showing peaks at  $234.6^{\text{[14]}}$  and  $231.4 \text{ eV}^{\text{[15]}}$  for  $\text{Mo}^{\text{V}}(3d_{3/2})$  and  $\text{Mo}^{\text{V}}(3d_{5/2})$ , respectively (Figure 2a,c). Based on XPS analysis, Mo in the as-synthesized **MoFeVO** and **MoFeO** was in the reduced state. Fe in the materials was in the mixed oxidation states with the peak positions at  $710.8^{\text{[16]}}$  and  $709.0 \text{ eV}^{\text{[17]}}$  ascribing to  $\text{Fe}^{\text{III}}(2p_{3/2})$  and  $\text{Fe}^{\text{II}}(2p_{3/2})$ . The ratios of  $\text{Fe}^{\text{III}}:\text{Fe}^{\text{II}}$  were 10 and 4 for **MoFeVO** and **MoFeO**, respectively (Figure 2e,g).  $\text{V}^{\text{V}}$  and  $\text{V}^{\text{IV}}$  coexisted in **MoFeVO**, and  $\text{V}^{\text{V}}:\text{V}^{\text{IV}}$  was 0.4 with the peaks at  $517.2^{\text{[18]}}$  and  $515.6 \text{ eV}^{\text{[19]}}$  for  $\text{V}^{\text{V}}$  and  $\text{V}^{\text{IV}}$  respectively (Figure 2i,k). There was no V peak being observed in **MoFeO** (Figure 2i). XPS demonstrated that Mo and V were reduced. The chemical formulae of the materials were estimated in Table S1.

Fourier transform infrared spectroscopy (FTIR) showed that the characteristic peaks of the as-synthesized (Figure S1Ba,b) **MoFeVO** and **MoFeO** at  $970, 754, 548,$  and  $522 \text{ cm}^{-1}$ . The FTIR spectra slightly changed with new shoulder peaks near ca.  $754 \text{ cm}^{-1}$  after incorporation of V, which indicating that V incorporation slightly changed the molecular structure.

The building unit of **MoFeVO** was the  $\epsilon$ -Keggin  $[\text{Fe}^{\text{III}}_{1.82}\text{Fe}^{\text{II}}_{0.18}\text{Mo}^{\text{V}}_{11.5}\text{V}^{\text{V}}_{0.3}\text{V}^{\text{IV}}_{0.7}\text{O}_{40}]^{12.38-}$  unit (Figure 1a), and the POM unit was connected with Fe or V in a tetrahedral manner to form the framework (Figure 1c). Based on the structural analysis, there were intrinsic micropores in **MoFeVO** and **MoFeO** (Figure 1c). The cavities were connected by the channels in a tetrahedral manner, and the channels were formed by six oxygen atoms with the diameter of ca.  $3.4 \text{ \AA}$ . The cavity was composed of ten POM units with the size of ca.  $7.7 \text{ \AA}$  (Figure 1c). The micropores were originally occupied by  $\text{Na}^+$  and water, which were opened by heat-treatment.  $\text{N}_2$  adsorption-desorption measurements were conducted for the materials (Figure S2a,b). The surface areas calculated by the BET method were  $25$  and  $29 \text{ m}^2/\text{g}$  for **MoFeVO** and **MoFeO**, respectively, and the external surface areas calculated by the t-plot method were  $19$  and  $19 \text{ m}^2/\text{g}$  for both materials, which

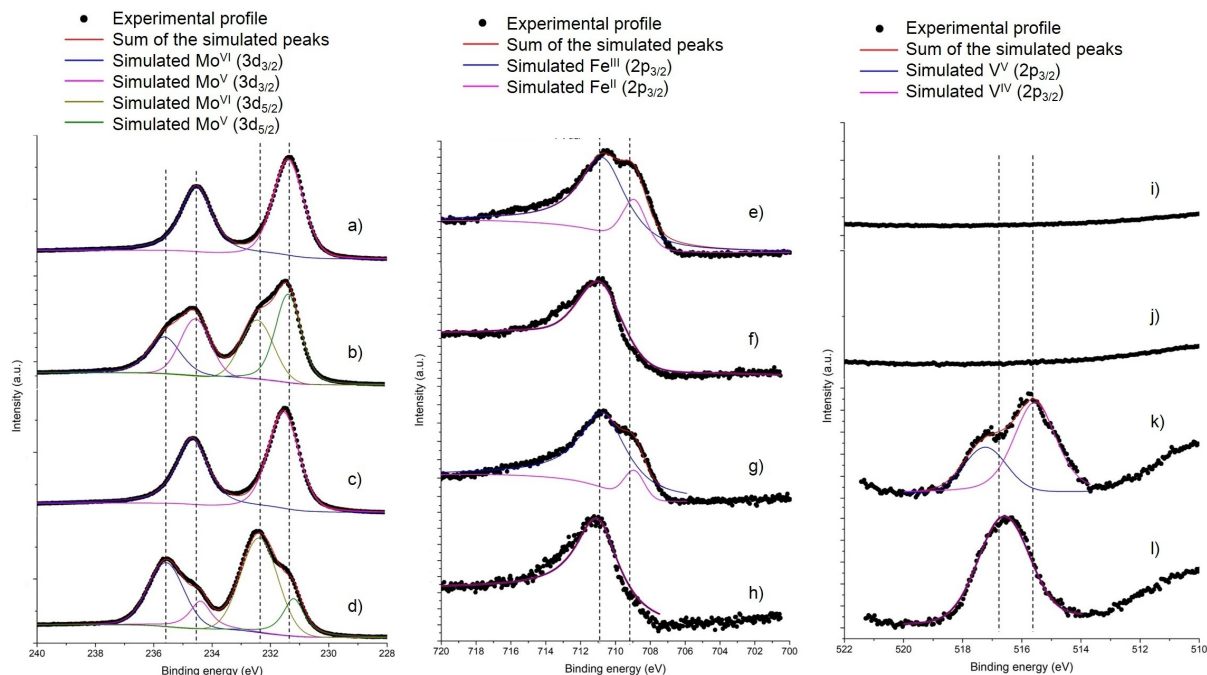


**Figure 2.** XPS profiles of Mo in a) **MoFeO**, b) **MoFeO** after  $O_2$  adsorption, c) **MoFeVO**, d) **MoFeVO** after  $O_2$  adsorption, Fe in e) **MoFeO**, f) **MoFeO** after  $O_2$  adsorption, g) **MoFeVO**, h) **MoFeVO** after  $O_2$  adsorption, V in i) **MoFeO**, j) **MoFeO** after  $O_2$  adsorption, k) **MoFeVO**, and l) **MoFeVO** after  $O_2$  adsorption,

were the same. Pore size distribution based on the SF method showed that the micropore size of **MoFeVO** was 0.61 nm and of **MoFeO** was 0.57 nm, respectively (Figure S2c).

**MoFeVO** and **MoFeO** were characterized by scanning electronic microscopy (SEM) and energy dispersive X-Ray spectroscopy (EDX) (Figure S3). As shown in the SEM-EDX elemental mapping images, V distributed in a **MoFeVO** particle, while there was no V in **MoFeO** being observed (Figure S3b,f). Mo and Fe uniformly distributed in **MoFeVO** and **MoFeO** (Figure S3c,d,g,h).

SEM showed that **MoFeVO** and **MoFeO** were polyhedral crystalline particle (Figure 3). Size distribution showed that the particle size of both materials was in the range of 20–160 nm. The distribution maximum was at 60–80 nm, which indicated that the size of the material was in nanoscale.

### Oxygen activation

**NH<sub>4</sub>MoFeO** was able to activate  $O_2$  at room temperature.<sup>[13]</sup>  $O_2$  adsorbed in **NH<sub>4</sub>MoFeO** with oxidation of Mo and Fe during the adsorption. The local structure of **NH<sub>4</sub>MoFeO** changed with changing the distance of Mo in the POM unit. However, the detailed factors on the  $O_2$  adsorption and activation were not investigated.

To understand the critical effects for  $O_2$  activation in the ZOMOs.  $O_2$  adsorption-desorption measurements were conducted. **MoFeVO** showed a unique  $O_2$  adsorption-desorption isotherm.  $O_2$  was adsorbed in the material, which was not able to be desorbed from the material, forming an irreversible adsorption-desorption isotherm (Figure S4). FTIR of **MoFeVO**

and **MoFeO** after  $O_2$  adsorption showed new peaks appeared at 798, 702, and 638  $cm^{-1}$  compared with the fresh materials. This indicated that the molecular structure changed after the  $O_2$  adsorption by oxidation of the material (Figure S1B). The XRD patterns showed that the basic structure of the materials did not change (Figure S1A).

There were three major factors for the unique  $O_2$  adsorption property, chemical composition, microporosity, and valence. Chemical compositions of the materials played an important role. Fe was critical for  $O_2$  activation at room temperature. Only Fe incorporated material showed the unique  $O_2$  adsorption isotherm. Sodium zinc molybdate (**NaMoZnO**) had the similar structure of **MoFeVO**, but no  $O_2$  adsorption was observed (Figure S4). Furthermore, the adsorbed amount of  $O_2$  in **MoFeVO** (ca. 8.8  $cm^3/g$ , 0.39 mmol/g) was higher than that in **MoFeO** (ca. 7.4  $cm^3/g$ , 0.33 mmol/g) (Figure S4b). V improved the redox activity of the material and caused more Mo to be oxidized during the  $O_2$  adsorption (Figure 2d). XPS showed the peaks at 235.6 and 234.4 eV for  $Mo^{VI}(3d_{3/2})$  and  $Mo^V(3d_{3/2})$ <sup>[20]</sup> and 232.4 and 231.2 eV for  $Mo^{VI}(3d_{5/2})$  and  $Mo^V(3d_{5/2})$ ,<sup>[21]</sup> in both materials (Figure 2b,d). The ratios of  $Mo^{VI}:Mo^V$  in **MoFeVO** and **MoFeO** was 3 and 0.75 (Table S1). Compared with XPS of the as-synthesized materials, the valence of Mo increased after the  $O_2$  adsorption, indicating that Mo was oxidized by  $O_2$ . More Mo was oxidized in **MoFeVO** than in **MoFeO**, which indicated that V incorporation promoted the redox capability during the  $O_2$  adsorption. Furthermore, Fe in both materials showed only a single peak at 710.8 eV for  $Fe^{III}$  after  $O_2$  adsorption, and V in **MoFeVO** was fully oxidized to  $V^V$ , which demonstrated that both Fe and V were oxidized. The chemical formulae of

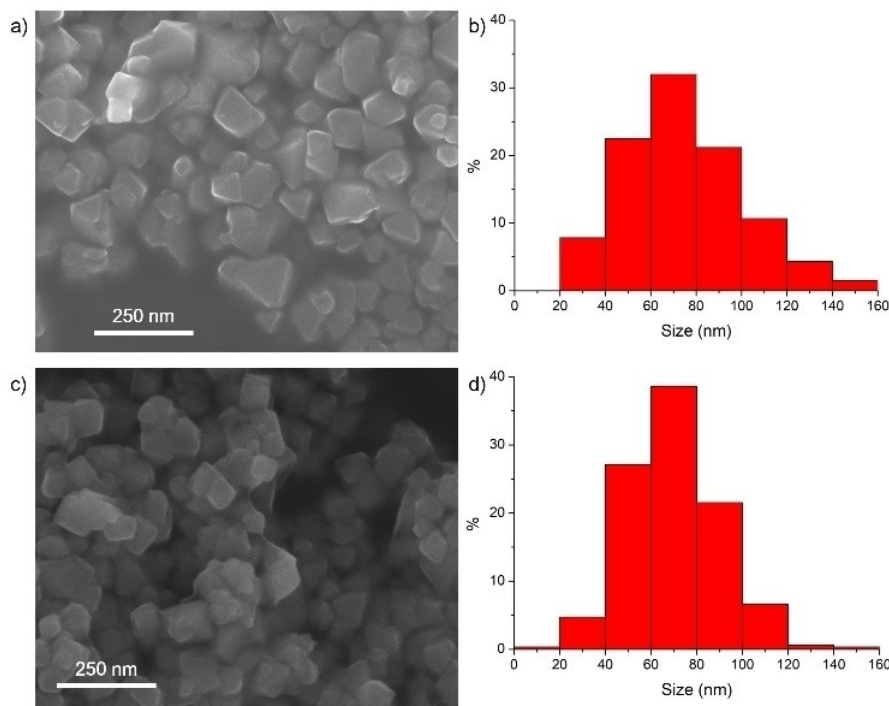


Figure 3. a) SEM image of MoFeO, b) size distribution of MoFeO, c) SEM image of MoFeVO, and d) size distribution of MoFeVO.

MoFeVO and MoFeO after O<sub>2</sub> adsorption were estimated in Table S1.

Microporosity was another factor for O<sub>2</sub> activation and adsorption. MoFeVO before heat-treatment showed low O<sub>2</sub> adsorption capacity (Figure S4), because the micropore was not fully opened. Furthermore, MoFeVO was heated at 400 °C in N<sub>2</sub>. The resulting material was denoted as MoFeVONC400. The structure of the material was damaged by the high temperature heat-treatment, as the XRD patterns and the FTIR spectra of the material changed after the heat-treatment (Figure S1A,Bh), while the valence of Mo might not change as the material was heated in N<sub>2</sub>. N<sub>2</sub> adsorption-desorption measurement confirmed there was no microporosity in MoFeVONC400 (Figure S2c). The material did not adsorb O<sub>2</sub> (Figure S4).

The O<sub>2</sub> adsorption behavior was dependent on the valence of metal in the material. When MoFeVO was pre-treated in O<sub>2</sub> at 200 °C, which was denoted as MoFeVOAC200, XRD showed that the crystal structure did not change (Figure S1 Ag). FTIR spectra showed that the peak at 754 cm<sup>-1</sup> for the reduced material disappeared while the peaks at 798, 702, and 638 cm<sup>-1</sup> for the oxidized material appeared (Figure S1B), which indicated that the material was oxidized. N<sub>2</sub> adsorption-desorption measurement showed that the material still had microporosity with the pore diameter of 0.63 nm (Figure S2c). The oxygen adsorption isotherm showed that MoFeVOAC200 did not adsorb O<sub>2</sub> anymore (Figure S4).

The redox properties of the materials were investigated by temperature programmed oxidation (TPO) and temperature programmed reduction (TPR). As shown in Figure 4, the materials started to be oxidized at 100 °C. There were two main

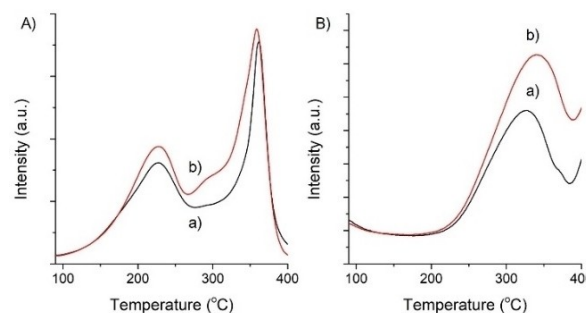


Figure 4. A) TPO profiles and B) TPR profiles of a) MoFeO and b) MoFeVO.

oxidation peaks at 200 °C and 350 °C, which might be attributed to the easily oxidized metal species and the hardly oxidized metal species. After incorporation of V in the structure, the peak area increased, which indicated that MoFeVO became more active to be oxidized. The reduction ability of the materials was investigated by TPR (Figure 4). Before the TPR measurement, the material was oxidized by O<sub>2</sub> at 200 °C. TPR showed that there was a single reduction peak starting at 200 °C with the peak maximum at 400 °C. The reduction peak of MoFeVO increased compared with that of MoFeO, which indicated that V increased the reduction ability.

### Catalytic reaction

MoFeVO and MoFeO were used as heterogeneous catalysts with tetrabutyl ammonium bromide (TBAB) and triethyl ammo-

nia (TEA) as the co-catalysts for the aerobic oxidation of the alcohols at 110 °C in toluene for 24 h. Before the reaction, **MoFeVO** and **MoFeO** were heated in air at 80 °C for 2 h to oxidize the materials, and the resulting materials were denoted as **MoFeVOAC80** and **MoFeOAC80**. The structures of the materials did not change during the treatment (Figure S1e). The reaction was carried out using *p*-methoxybenzyl alcohol as a model substrate. *p*-Methoxybenzyl alcohol was converted to *p*-methoxybenzaldehyde with 92% of selectivity and 99% of conversion of the alcohol (Table 1, entry 1).

Chemical composition affected the catalytic activity. The iso-structural ZOMOs based on different  $\epsilon$ -Keggin POMs were used for *p*-Methoxybenzyl alcohol oxidation. Zinc molybdate (**NaMoZnO** and **NH<sub>4</sub>MoZnO**),<sup>[12]</sup> manganese molybdate (**MoMnO**),<sup>[12]</sup> and cobalt molybdate (**MoCoO**)<sup>[22]</sup> were synthesized. All ZOMOs were heated at 80 °C for 2 h before the reaction, and the resulting materials were denoted as **NaMoZnOAC80**, **MoMnOAC80**, **MoCoOAC80**, and **NH<sub>4</sub>MoZnOAC80**. As shown in Table 1, **MoFeVOAC80** showed a high catalytic activity, and high alcohol conversion and aldehyde selectivity were achieved. Furthermore, V improved the catalytic activity. Compared with **MoFeVOAC80**, **MoFeOAC80** showed a slightly lower alcohol conversion with similar aldehyde selectivity (Table 1, entries 1, 2). Cation affected the catalytic activity of the catalysts. When the cation was changed from Na<sup>+</sup> to NH<sub>4</sub><sup>+</sup>, the catalytic activity decreased (Table 1, entries 3, 4). Fe was critical for the high activity of the reaction, and only the Fe incorporated materials, **MoFeOAC80** and **MoFeVOAC80**, were active for the reaction (Table 1). When ZOMOs without Fe, such as **MoZnOAC80**, **MoMnOAC80**, and **MoCoOAC80**, were used for the reaction the activity was low, which demonstrated that Fe was the key element for the selective oxidation (Table 1, entries 1–8). Simple metal oxides, such as MoO<sub>3</sub>, V<sub>2</sub>O<sub>5</sub>, and Fe<sub>3</sub>O<sub>4</sub>, were not active for the reaction (Table 1, entries 10–12). Without the catalyst and the co-catalysts no product was obtained (Table 1, entry 11).

Furthermore, ion-exchange was able to replace the cation species of the material, which would change the property of the material. According to the previous study, Fe-exchange

would enable the material for the O<sub>2</sub> activation.<sup>[13]</sup> Herein, we found that introducing Fe by the ion-exchange process would enhance the catalytic activity of the material. Compared with the catalytic activity of **NH<sub>4</sub>MoZnOAC80** (Table 1, entry 8), the Fe exchanged **NH<sub>4</sub>MoZnO** (**Fe–NH<sub>4</sub>MoZnOAC80**) was more active (Table 1, entry 9). However, the catalytic activity of **Fe–NH<sub>4</sub>MoZnOAC80** was still lower than that of **MoFeVOAC80** and **MoFeOAC80**. This might be due to the lower Fe amount incorporated by the ion-exchange process and also the different positions of Fe in the materials. Fe was only in the cation site of **Fe–NH<sub>4</sub>MoZnOAC80** and not in the framework.

The catalytic activity of **MoFeVO** changed with different pre-treatment conditions (Table S2, entry 1). The activity of the as-synthesized **MoFeVO** was low (Table S2, entry 2). The material became active when it was heat at 80–200 °C in air, which indicated that oxidation of the material would increase the catalytic activity of the material (Table S2, entries 2–4). Further heating at 400 °C would damage the crystal structure of the material and the catalyst became inactive (Table S2, entry 5).

The co-catalysts, TBAB and TEA, were important for the reaction. Without the co-catalysts the conversion of the alcohol was still high, but the selectivity to the aldehyde was low (Table S3). Gas Chromatograph Mass (GC-MS) confirmed that some by-products were derived from alkylation catalyzed by acids (Figure S5), and therefore adding basic compound (TEA) could effectively suppress the side-reactions. However, almost no aldehyde was obtained only using the co-catalysts.

Solvent effect of **MoFeVOAC80** was investigated. As shown in Table S4, toluene was a good solvent for this reaction. High conversion of the alcohol and selectivity to the aldehyde were obtained (Table S4, entry 1). In other aromatic hydrocarbon solvents, the selectivity to the aldehyde was high while the alcohol conversion was low (Table S4, entries 2–5). The reaction in the polar solvent, N-methyl pyrrolidone (NMP) showed a lower conversion and selectivity (Table S4, entry 6).

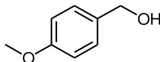
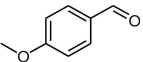
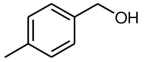
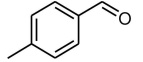
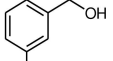
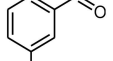
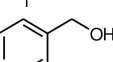
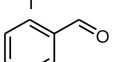
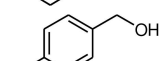
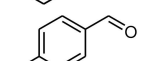
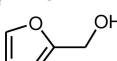
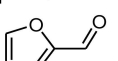
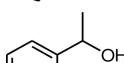
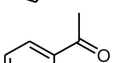
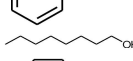
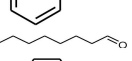
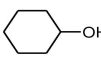
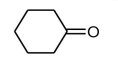
Other factors of the reaction were also investigated. The dosage of the catalyst affected the catalytic activity. Catalytic activity increased with the catalyst amount increasing. The conversion of the alcohol reached to 99% with >90% of selectivity using 0.04 g of the catalyst (Figure S6a). When the reaction was run at a temperature below 55 °C, no conversion was observed (Figure S6b). When the reaction temperature increased to 110 °C, the reaction became active. The conversion of the alcohol increased with the reaction time prolonged, and the selectivity to the aldehyde kept most the same and above 90% (Figure S6c).

**MoFeVOAC80** was able to oxidize a variety of different primary aromatic alcohols with air as the oxidant in toluene at 110 °C. High conversion of the alcohol and high selectivity to the aldehyde were obtained, such as *p*-methoxybenzyl alcohol, 4-methylbenzyl alcohol, and 3-methylbenzyl alcohol, benzyl alcohol, and 4-bromo benzyl alcohol (Table 2, entries 1–5). Furfuralcohol, as a heterocyclic aromatic alcohol, was able to be converted to form furfural (Table 2, entry 6). **MoFeVOAC80** showed almost no catalytic activity for the secondary aromatic alcohol such as  $\alpha$ -phenylethanol, which might be due to the weaker interaction of the compound with the catalysts (Table 2,

**Table 1.** *p*-Methoxybenzyl alcohol oxidation catalyzed by different catalytic materials with air.<sup>[a]</sup>

Entry	Catalyst	Conv. [%]	Yield [%]	Sel. [%]
1	<b>MoFeVOAC80</b>	99	92	92
2	<b>MoFeOAC80</b>	88	87	99
3	<b>NH<sub>4</sub>MoFeVOAC80</b>	91	67	74
4	<b>NH<sub>4</sub>MoFeOAC80</b>	72	66	92
5	<b>NaMoZnOAC80</b>	12	12	99
6	<b>MoMnOAC80</b>	21	10	48
7	<b>MoCoOAC80</b>	15	6	40
8	<b>NH<sub>4</sub>MoZnOAC80</b>	8	8	99
9	<b>Fe–NH<sub>4</sub>MoZnOAC80</b>	29	27	93
10	MoO <sub>3</sub>	80	25	25
11	V <sub>2</sub> O <sub>5</sub>	99	69	69
12	Fe <sub>3</sub> O <sub>4</sub>	0	0	0
13	–	2	0	–

[a] Reaction conditions: catalyst: 0.04 g, *p*-methoxybenzyl alcohol: 0.8 mmol, TBAB: 0.01 g (0.0311 mmol), TEA: 0.01 mL (0.0721 mmol), toluene: 0.5 mL, decane: 0.05 mL, temperature: 110 °C, time: 24 h.

Entry	Substrate	Product	Conv. [%]	Y. [%]	Sel. [%]
1			99	92	92
2			62	62	99
3			81	80	99
4			84	78	93
5			99	93	93
6			72	53	74
7			0	0	–
8			0	0	–
9			0	0	–

[a] Reaction conditions: MoFeVO: 0.04 g, alcohol: 0.8 mmol, TBAB: 0.01 g (0.0311 mmol), TEA: 0.01 mL (0.0721 mmol), toluene: 0.5 mL, decane: 0.25 mmol, temperature: 110 °C, time: 24 h.

entry 7), and it was discussed in a later part. Besides the secondary aromatic alcohol. The material also could not oxidize alkanol and cyclic alcohol (Table 2, entries 8,9).

Stability of MoFeVOAC80 was evaluated by the recycling experiment (Figure 5). After the reaction, the catalyst was separated by centrifugation (see the experimental part) and dried for the next cycle directly. The catalyst showed a stable catalytic activity, which was reused for 5 times without loss of the catalytic activity. The yield and selectivity to the aldehyde

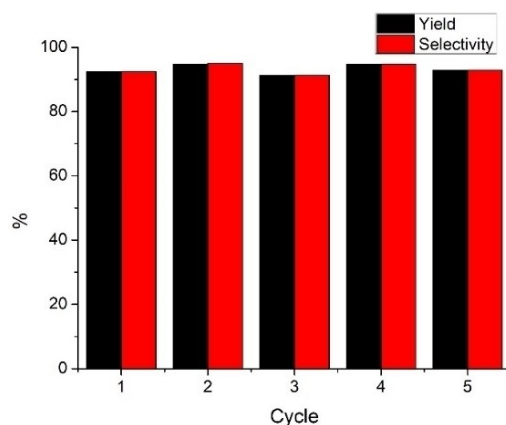


Figure 5. Reusability of MoFeVO for alcohol oxidation, Reaction conditions: MoFeVO: 0.04 g, *p*-methoxybenzyl alcohol: 0.8 mmol, TBAB: 0.01 g (0.0311 mmol), TEA: 0.01 mL (0.0721 mmol), toluene: 0.5 mL, decane: 0.25 mmol, temperature: 110 °C, time: 24 h.

kept over 90%. The reused catalyst for 5 times was characterized by FTIR, which indicated that the material was oxidized, as the FTIR peaks at 798, 702, and 638  $\text{cm}^{-1}$  for the oxidized material was observed (Figure S1B and Figure S7). XPS of MoFeVOAC80 before and after the reaction also showed that Mo and V were oxidized after the reaction (Figure S8). The material after the reaction still showed the microporosity (Figure S2). The XRD patterns of the material showed that the basic structure of the material did not change after the reaction, which indicated that the material was stable (Figure S7).

MoFeVOAC80 was tested by the filtration experiment. As shown in Table S5, the reaction was conducted with the catalyst for 5 h. The catalyst was then removed by centrifugation. The filtrate was heated at 110 °C for the rest 19 h, showing that the conversion of the alcohol was 28%. Compared with the reaction with the catalyst for 24 h, the conversion of the alcohol after removal of the catalyst was remarkably lower than that of the reaction with the catalyst, which indicated that MoFeVO was a heterogeneous catalyst (Figure 3).

The conversion of the alcohol was plotted against the time at different temperatures. When the reaction time increased the conversion of the alcohol increased. As shown in Figure S6c, there was a linear relationship between the conversion and the reaction time, which demonstrated that the apparent order of the alcohol was close to 0. Thus, we assumed that the oxidation was a surface reaction. The adsorption of the alcohol molecule on the surface of the catalyst was a fast step. The apparent activation energy of the reaction was calculated based on the kinetic data using the Arrhenius equation to be 94 kJ/mol (Figure S9).

Because of the surface reaction, the interaction of the alcohol molecule and the catalyst surface was investigated. The surface active site would catalyze the reaction. Transmission electron microscopy (TEM) image showed that the external surface of the material was the (1 1 1) plane (Figure 6a), which was constructed by the  $\epsilon$ -Keggin POM units with linkers (Figure 6b). The cavity and channel would also exist on the external surface. The surface cavity formed by 12 oxygen atoms with the size of ca. 7.7 Å in the diameter. The channel was surrounded by 6 oxygen atoms with the diameter of ca. 3.4 Å (Figure 6b). The size of benzyl alcohol was estimated to be 6.5 Å, which was smaller than the cavity but larger than the channel. The surface cavity was open and accessible to the alcohol while the channel was too small for the alcohol to enter the bulk. Therefore, we assumed that the (1 1 1) plane on the surface interacted with the alcohol and catalyzed the reaction.

The Monte-Carlo simulation showed that the aromatic alcohol adsorbed on the external surface of the catalyst, which located in the cavity on the surface and not enter the bulk of the material. The hydroxymethyl group interacted with the cation species on the external surface, and the cation located in the cage on the surface of the material (Figure 6c). Using benzyl alcohol and  $\alpha$ -phenylethanol as probe molecules caused different results. The system energy of benzyl alcohol based system (–18.56 kcal/mol) was lower than that of  $\alpha$ -phenylethanol based system (–17.07 kcal/mol), which indicated that the material had a stronger interaction with benzyl alcohol than  $\alpha$ -

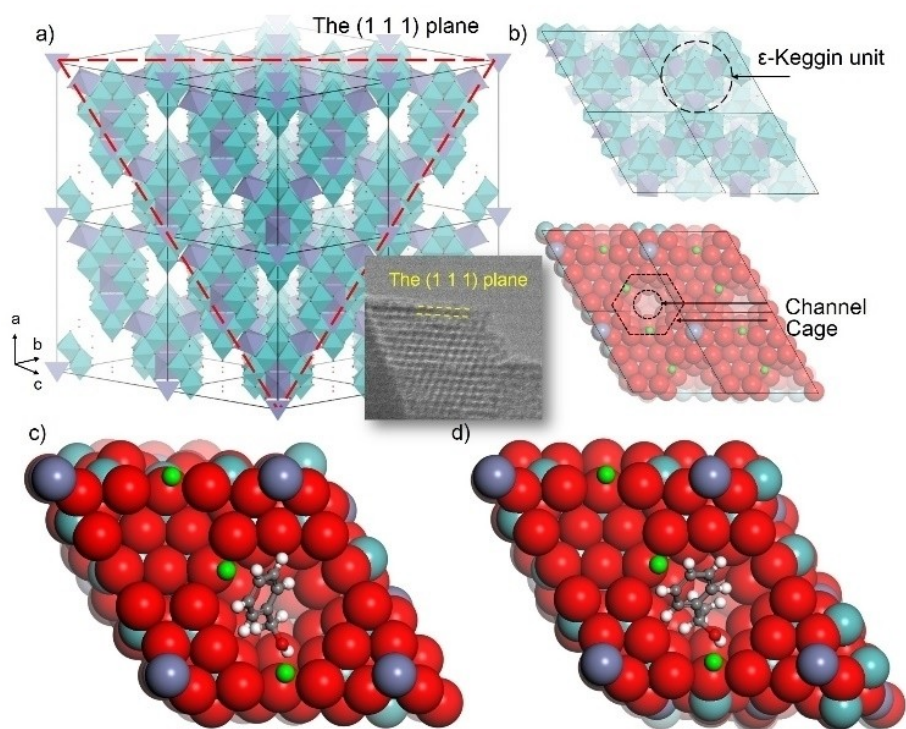


**Figure 6.** a) Polyhedral representation of unit cell of the material, inserted image: TEM image of the material showing the (1 1 1) plane of the material, b) polyhedral representation (up) and CPK representation (down) of the (1 1 1) plane of the material, c) benzyl alcohol adsorbed on the (1 1 1) plane of the material, and d)  $\alpha$ -methylbenzyl alcohol adsorbed on the (1 1 1) plane of the material, Mo (blue), Fe (purple), O (red), C (black), H (white), Na (green).

phenylethanol. The larger volume of hydroxyethyl group of  $\alpha$ -phenylethanol might cause the weaker interaction with the cage. The weaker interaction of the secondary aromatic alcohol would make its reactivity low, which would be the reason for the low activity for  $\alpha$ -phenylethanol (Table 2, entry 7). Furthermore,  $\text{Na}^+$  in the catalyst and H in the alcohol were positively charged and O in the catalyst and the alcohol was negatively charged. There was electrostatic interaction between the catalyst and the alcohol, which would be important for the reaction. After  $\text{Na}^+$  ( $\text{MoFeVO}$ ) was changed to  $\text{NH}_4^+$  ( $\text{NH}_4\text{MoFeVO}$ ), the catalytic activity decreased (Table 1, entries 8, 9), which indicated that the interaction of the cation and the alcohol was important.

When the alcohol was adsorbed on the surface of the material the redox reaction occurred. The adsorbed alcohol was oxidized by  $\text{MoFeVOAC80}$ . The reaction was carried out without the existence of  $\text{O}_2$  at  $110^\circ\text{C}$  for 24 h. The result showed that there a small amount of the alcohol converted to the aldehyde (ca. 9%), which indicated that the material oxidized the alcohol. Furthermore, the resulting  $\text{MoFeVOAC80}$  was characterized by FTIR (Figure S10). The peak for oxidized material ( $798$  and  $702\text{ cm}^{-1}$ ) decreased and the peak for the reduced material ( $754\text{ cm}^{-1}$ ) increased compared with FTIR of  $\text{MoFeVOAC80}$  and  $\text{MoFeVO}$  (Figure S10a,b), which indicated that  $\text{MoFeVOAC80}$  was reduced.

After oxidation of the alcohol,  $\text{MoFeVOAC80}$  was reduced. The reduced  $\text{MoFeVOAC80}$  was re-oxidized by  $\text{O}_2$  for the next catalytic cycle.  $\text{MoFeVO}$  was able to be oxidized by  $\text{O}_2$  at a low

temperature even room temperature (Figure S4), while the alcohol oxidation did not occur at a temperature below  $55^\circ\text{C}$  (Figure S6b). The re-oxidation of the catalyst might be faster than the oxidation of the alcohol. Therefore, we assumed that the slow step of the reaction was the oxidation of the adsorbed alcohol to form the aldehyde by the catalyst.

Based on the above discussion, the reaction pathway of the alcohol oxidation catalyzed by  $\text{MoFeVOAC80}$  was proposed. Firstly, the alcohol adsorbed on the external cavity of the material. Then, the adsorbed alcohol was oxidized by the material to form the aldehyde and the reduced material. Finally, the reduced material was re-oxidized by  $\text{O}_2$  at a certain temperature without change of the structure for the next cycle.

## Conclusion

In summary, zeolitic iron vanadomolybdates was synthesized as the catalyst for the aerobic oxidation of alcohols under a mild condition. Oxygen activation in the micropore of the material. Oxygen oxidized Mo in the material. V incorporation improved the redox reaction. More Mo was oxidized in  $\text{MoFeVO}$ . The material was used as one catalyst for the oxidation of alcohols using air as an oxidant. Different primary aromatic alcohols can be oxidized to form corresponding aldehydes with high conversion and selectivity. The material can be recovered and reused without losing activity. The material showed different activities for primary alcohols and secondary alcohols, which

might be due to the active site confine the molecules interacted with material.

## Experimental Section

### Material synthesis

Synthesis of **MoFeO** and **MoFeVO**:  $\text{Na}_2\text{MoO}_4 \cdot 2\text{H}_2\text{O}$  (8.75 mmol based on Mo for **MoFeO** and 7.88 mmol based on Mo for **MoFeVO**) and  $\text{NaVO}_3$  (0.87 mmol based on V only for **MoFeVO**), were dissolved in 40 mL of distilled water. Metal Mo (0.150 g, 1.56 mmol) and  $\text{Fe}_3\text{O}_4$  (0.194 g, 0.83 mmol) were added to the mixture sequentially. The mixture was acidified by 6 mL of sulfuric acid (10 g of sulfuric acid to 100 mL of water). The mixture was introduced into a 50-mL of a stainless-steel autoclave with a Teflon liner. The autoclave was fixed in an oven with a mechanical rotation system. Hydrothermal synthesis was performed at 175 °C with tumbling (4 rpm) for 48 h. After the autoclave had been cooled down, the crude solid was moved to a 100 mL-beaker and 60 mL of water was added. The un-reacted  $\text{Fe}_3\text{O}_4$  was completely removed by a magnet. The resulting suspension was centrifuged (3500 rpm, 30 min), and solids on the bottom of the centrifugation tube were collected. The collected solid was washed with water by dispersing in 10 mL of water and subsequent centrifugation (3500 rpm, 30 min). After the washing process was repeated two more times, the obtained solid was dried. The resulting 0.995 g and 0.509 g of **MoFeO** and **MoFeVO**, were obtained with the yields of 62% and 36% based on Mo, respectively. Elemental analysis for  $\text{NaH}_{11.38}[\text{Fe}_2\text{Mo}_{11.5}\text{V}_1\text{O}_{40}] \cdot 12\text{H}_2\text{O}$  Calc Na, 1.09; Mo, 52.40; Fe, 5.31; V, 2.24, found Na 1.16, Mo 53.03, Fe 4.95, V 1.99. Elemental analysis for  $\text{Na}_{1.5}\text{H}_{11.5}[\text{Fe}_{2.5}\text{Mo}_{12}\text{O}_{40}] \cdot 8.5\text{H}_2\text{O}$  Calc Na, 1.62; Mo, 54.05; Fe, 6.56, found Na, 1.46; Mo, 54.40; Fe, 7.05.

### Synthesis of other materials

Synthesis of other materials based on  $\epsilon$ -Keggin POM unit, such as **NaMoZnO**, **NH<sub>4</sub>MoZnO**<sup>[12]</sup>, **MoMnO**<sup>[12]</sup> and **MoCoO**<sup>[22]</sup> were on the basis of the previous methods. Fe exchange experiment was carried out at room temperature in aqueous solution for **NH<sub>4</sub>MoZnO**, which was also according to the previous method.<sup>[13]</sup>

### Characterizations

XRD patterns were recorded on a Bruker, D8 Advance with Cu–K $\alpha$  radiation (tube voltage: 40 kV, tube current: 40 mA). FT-IR was conducted on a Bruker Vertex 70. XPS was performed on Thermo Scientific K-Alpha. The spectrometer energies were calibrated using the C<sub>1s</sub> peak at 284.7 eV. SEM image and EDX were obtained with Nova Nano 450. TEM image was taken with a 200 kV TEM (JEOL JEM-2100F). Elemental analysis was measured in the analysis center of School of Material Science and Chemical Engineering, Ningbo University. GC-MS was carried out on an Agilent 7890B with Agilent 5977B MSD.

Gas adsorption-desorption measurements were performed on **MoFeO** and **MoFeVO** by a Micromeritics 3flex sorption analyzer. The samples were evacuated at 200 °C for 2 h before the measurement. N<sub>2</sub> adsorption-desorption measurements were carried out at –196 °C, and O<sub>2</sub> adsorption-desorption measurements were carried out at 25 °C.

TPO measurements were carried out on a BelcatII. Before the measurements, the material was pre-treated at 200 °C for 1 h under He flow (50 mL/min). The temperature was increased from 80 °C to

600 °C with a ramp of 10 °C/min under O<sub>2</sub> flow (10% of O<sub>2</sub> in He, 20 mL/min). The signal was monitored by TCD. TPR measurements were carried out on a BelcatII. Before the measurements, the material was pre-treated at 200 °C for 1 h under O<sub>2</sub> flow (10% of O<sub>2</sub> in He, 50 mL/min). The temperature was increased from 80 °C to 600 °C with a ramp of 10 °C/min under H<sub>2</sub> flow (10% of H<sub>2</sub> in Ar, 20 mL/min). The signal was monitored by TCD.

### Catalytic reactions

The reaction was carried out on the flask with condenser. Typically, catalyst (0.04 g), TBAB (0.01 g, 0.031 mmol), TEA (0.01 mL, 0.072 mmol), *p*-methoxybenzyl alcohol (0.1 mL, 0.8 mmol), decane (0.05 mL, 0.25 mmol), and toluene (0.5 mL) were added to the flask. The mixture was heated at 110 °C for 24 h. After the reaction finished and the mixture had been cooled under, the solution was analyzed by GC-FID, and conversion and selectivity were calculated.

For cycle-recovery experiment, the catalyst was recovered by centrifugation (10000 rpm, 5 min) after the reaction. The catalyst was washed with ethanol for 3 times, which was dried at room temperature under high vacuum overnight for the next cycle.

### Simulation

Monte-Carlo simulation was performed to predict the adsorbed structure of the alcohol molecule on the surface of the catalyst. Before the Monte-Carlo simulation, the structure of the material was optimized based on the previous study using **NaMoZnO**<sup>[23]</sup> which was an iso-structural material of **MoFeVO**, as a model structure by geometry optimization using the DMol<sup>3</sup> program<sup>[24]</sup> in the Materials studio package. The Perdew-Burke-Ernzerhof (PBE) generalized gradient functional and DND basis set were used for calculation. The calculated Mulliken atomic charge was applied for the Monte-Carlo simulation. The structures of the framework of the material, benzyl alcohol, and phenethyl alcohol, were optimized before the Monte-Carlo simulation. The Monte-Carlo simulation was carried out with the adsorption locator program in the Materials studio package. The guest molecules were introduced into the framework of the material one by one.

## Acknowledgements

This work was financially supported by the National Natural Science Foundation of China (Grant No. 21801141, 21622607, 21761132009, 22075153, and 22006077), the Natural Science Foundation of Ningbo (Grant No. 2019A610020 and 2019A610452), National Natural Science Foundation of Zhejiang (No. LR18B060002), Major Special Projects of the Plan "Science and Technology Innovation 2025" in Ningbo (No. 2018B10016), and the K. C. Wong Magna Fund in Ningbo University.

## Conflict of Interest

The authors declare no conflict of interest.

**Keywords:** zeolitic transition metal oxide · redox property · selective oxidation · microporosity

- [1] a) D. Wang, A. B. Weinstein, P. B. White, S. S. Stahl, *Chem. Rev.* **2018**, *118*, 2636–2679; b) G. T. E. N. Brink, Å. Dijkstra, *Acc. Chem. Res.* **2002**, *35*, 774–781; c) T. Mallat, A. Baiker, *Chem. Rev.* **2004**, *104*, 3037–3058.
- [2] a) M. Bron, R. Holze, *Surf. Sci.* **2000**, *457*, 178–184; b) W. Koo-amornpattana, J. M. Winterbottom, *Catal. Today* **2001**, *66*, 277–287; c) T. Mallat, Z. Bodnar, A. Baiker, in *Heterog. Catal. Fine Chem. III* (Eds.: M. Guisnet, J. Barbier, J. Barrault, C. Bouchoule, D. Duprez, G. Pérot, C. B. T.-S. in S. S. and C. Montassier), Elsevier, **1993**, pp. 377–384; d) Y. Xu, J. Li, J. Zhou, Y. Liu, Z. Wei, H. Zhang, *J. Catal.* **2020**, *389*, 409–420.
- [3] a) H. Ji, T. Mizugaki, K. Ebitani, K. Kaneda, *Tetrahedron Lett.* **2002**, *43*, 7179–7183; b) B.-Z. Zhan, M. A. White, T.-K. Sham, J. A. Pincok, R. J. Doucet, K. V. R. Rao, K. N. Robertson, T. S. Cameron, *J. Am. Chem. Soc.* **2003**, *125*, 2195–2199; c) F. Sabaté, J. L. Jordá, M. J. Sabater, A. Corma, *J. Mater. Chem. A* **2020**, *8*, 3771–3784.
- [4] K. Otake, Y. Cui, C. T. Buru, Z. Li, J. T. Hupp, O. K. Farha, *J. Am. Chem. Soc.* **2018**, *140*, 8652–8656.
- [5] a) T. L. Stuchinskaya, I. V. Kozhevnikov, *Catal. Commun.* **2003**, *4*, 417–422; b) C.-B. Wang, Y. Cai, I. E. Wachs, *Langmuir* **1999**, *15*, 1223–1235; c) P. Deshlahra, E. Iglesia, *J. Phys. Chem. C* **2014**, *118*, 26115–26129.
- [6] a) F. Wang, W. Ueda, *Appl. Catal. A* **2008**, *346*, 155–163; b) R. Neumann, M. Levin, *J. Org. Chem.* **1991**, *56*, 5707–5710.
- [7] a) S. G. Mitchell, C. Streb, H. N. Miras, T. Boyd, D.-L. Long, L. Cronin, *Nat. Chem.* **2010**, *2*, 308–312; b) S. G. Mitchell, T. Boyd, H. N. Miras, D.-L. Long, L. Cronin, *Inorg. Chem.* **2011**, *50*, 136–143; c) C. Zhan, J. M. Cameron, D. Gabb, T. Boyd, R. S. Winter, L. Vilà-Nadal, S. G. Mitchell, S. Glatzel, J. Breternitz, D. H. Gregory, et al., *Nat. Commun.* **2017**, *8*, 14185; d) M. I. Khan, L. M. Meyer, R. C. Haushalter, A. L. Schweitzer, J. Zubieta, J. L. Dye, *Chem. Mater.* **1996**, *8*, 43–53; e) D. Liu, Y. Lu, H.-Q. Tan, W.-L. Chen, Z.-M. Zhang, Y.-G. Li, E.-B. Wang, *Chem. Commun.* **2013**, *49*, 3673–3675.
- [8] a) M. Sadakane, K. Yamagata, K. Kodato, K. Endo, K. Toriumi, Y. Ozawa, T. Ozeki, T. Nagai, Y. Matsui, N. Sakaguchi, et al., *Angew. Chem. Int. Ed.* **2009**, *48*, 3782–3786; b) L. Annamalai, S. Ezenwa, Y. Dang, H. Tan, S. L. Suib, P. Deshlahra, *Catal. Today* **2020**, *In press*, 10.1016/j.cattod.2020.04.046; c) Y. Liu, L. Annamalai, P. Deshlahra, *J. Phys. Chem. C* **2019**, *123*, 28168–28191; d) L. Annamalai, Y. Liu, S. Ezenwa, Y. Dang, S. L. Suib, P. Deshlahra, *ACS Catal.* **2018**, *8*, 7051–7067.
- [9] Z. Zhang, M. Sadakane, M. Hara, W. Ueda, *Chem. Eur. J.* **2017**, *23*, 17497–17503.
- [10] Z. Zhang, Q. Zhu, M. Sadakane, T. Murayama, N. Hiyoshi, A. Yamamoto, S. Hata, H. Yoshida, S. Ishikawa, M. Hara, et al., *Nat. Commun.* **2018**, *9*, 3789.
- [11] Z. Zhang, M. Sadakane, T. Murayama, S. Izumi, N. Yasuda, N. Sakaguchi, W. Ueda, *Inorg. Chem.* **2014**, *53*, 903–911.
- [12] Z. Zhang, M. Sadakane, T. Murayama, N. Sakaguchi, W. Ueda, *Inorg. Chem.* **2014**, *53*, 7309–7318.
- [13] Z. Zhang, S. Ishikawa, Q. Zhu, T. Murayama, M. Sadakane, M. Hara, W. Ueda, *Inorg. Chem.* **2019**, *58*, 6283–6293.
- [14] K. Isao, M. Gen-etsu, *Bull. Chem. Soc. Jpn.* **1994**, *67*, 694–698.
- [15] I. Kawafune, G. Matsubayashi, *Inorg. Chim. Acta* **1991**, *188*, 33–39.
- [16] M. Oku, K. Hirokawa, *J. Electron Spectrosc. Relat. Phenom.* **1976**, *8*, 475–481.
- [17] W. A. Brainard, D. R. Wheeler, *J. Vac. Sci. Technol.* **1978**, *15*, 1800–1805.
- [18] W. E. Slink, P. B. DeGroot, *J. Catal.* **1981**, *68*, 423–432.
- [19] B. Horvath, J. Strutz, J. Geyer-Lippmann, E. G. Horvath, *Z. Anorg. Allg. Chem.* **1981**, *483*, 181–192.
- [20] M. Anwar, C. A. Hogarth, R. Bulpett, *J. Mater. Sci.* **1989**, *24*, 3087–3090.
- [21] J. E. deVries, H. C. Yao, R. J. Baird, H. S. Gandhi, *J. Catal.* **1983**, *84*, 8–14.
- [22] T. Igarashi, Z. Zhang, T. Haioka, N. Iseki, N. Hiyoshi, N. Sakaguchi, C. Kato, S. Nishihara, K. Inoue, A. Yamamoto, et al., *Inorg. Chem.* **2017**, *56*, 2042–2049.
- [23] Z. Zhang, M. Sadakane, S. Noro, T. Murayama, T. Kamachi, K. Yoshizawa, W. Ueda, *J. Mater. Chem. A* **2015**, *3*, 746–755.
- [24] a) B. Delley, *J. Chem. Phys.* **2000**, *113*, 7759–7764; b) B. Delley, *J. Chem. Phys.* **1990**, *92*, 508–517.

---

Manuscript received: October 18, 2020  
Revised manuscript received: December 6, 2020  
Accepted manuscript online: January 15, 2021  
Version of record online: February 18, 2021